Rock Mech Rock Eng (2017) 50:1337–1346
DOI 10.1007/s00603-016-1162-2

TECHNICAL NOTE

Dominant Frequency Characteristics of Acoustic Emissions in White Marble During Direct Tensile Tests

L. R. Li[1] · J. H. Deng[1] · L. Zheng[2] · J. F. Liu[1]

Received: 18 July 2016 / Accepted: 29 December 2016 / Published online: 17 January 2017

Keywords Dominant frequency · Acoustic emission · Direct tensile · White marble · Statistical analysis · Failure mechanism

1 Introduction

Acoustic emission (AE) is defined as elastic waves associated with a rapid release of localized stress energy that is propagated within a material. It has been proven to be a useful tool for studying rock fractures (e.g., Lavrov 2003; Prikry et al. 2003; Tham et al. 2005; Amann et al. 2011; Shukla et al. 2013; Liu et al. 2015; Moradian et al. 2016; Zhang et al. 2016). Parametric and waveform data are two basic forms of recordable AE data. In the past few decades, parameter analysis has been widely used to observe progressive damage processes resulting from AE, as well as to evaluate the degree of damage (e.g., Butt 1999; Baddari et al. 2011; Xie et al. 2011; Zhao et al. 2013; Zhang et al. 2015). However, a single complicated AE waveform still might conceal important information, or may even present misleading information, since it is discriminated by only a few parameters (Behnia et al. 2014). Thus, it may be difficult to adequately discriminate the characteristics of AE waveforms using such parameter-based approaches.

✉ L. Zheng
zhenglu@scu.edu.cn

[1] State Key Laboratory of Hydraulics and Mountain River Engineering, College of Water Resources and Hydropower, Sichuan University, Chengdu 610065, Sichuan, China

[2] Institute for Disaster Management and Reconstruction, Sichuan University, Chengdu 610065, China

In waveform-based approaches, spectral analysis methods are often used for signal waveforms analyses. Because frequency content in an AE is determined by the wave source, studying the dominant frequency characteristics provides significant controls on investigations of microscopic fractures. Some of the pioneering work that investigated the dominant frequency characteristics of rocks was performed based on spectral analysis (e.g., Chugh et al. 1968; Armstrong 1969). Later, numerous relevant studies were conducted that evaluated the dominant frequency characteristics of AE waveforms (e.g., Stephens and Pollock 1971; Fleischmann et al. 1975; Woodward 1976; Kranz 1979; Sondergeld et al. 1980; Read et al. 1995; Xu et al. 2010). Owing to both hardware and software restrictions, it was impossible to realize continuous sampling, digitization and storage of a large quantity of AE waveforms within a short time. Previous studies did not contain statistical analyses and mainly focused on the change of dominant frequency characteristics since few waveforms could be recorded.

With the development of high-performance computational processors and a new generation of sensors, the acquisition of multichannel raw waveforms has become possible (Behnia et al. 2014) and benefits the statistical analysis of the dominant frequency characteristics of AE waveforms. However, some latest studies about the dominant frequency of AE waveforms (Lu et al. 2013; Reiweger et al. 2015) still did not involve the statistical analysis. Ohnaka and Mogi (1981, 1982) expounded on the importance of statistical analysis for investigating the dominant frequency characteristics of AE waveforms. Moreover, statistical characteristics of dominant frequency of AE waveforms may be beneficial to understand the microscopic failure mechanism of rock.

The objective of this paper is to present the dominant frequency characteristics of AE waveforms of marble samples acquired during direct tensile tests, and then briefly discuss the relationship between the microscopic failure mechanism and the statistical characteristics. For this purpose, an improved processing method was proposed. AE waveforms for eight tested samples were obtained and analyzed. The amplitude characteristics of the AE waveforms were presented and discussed for various stress stages. The characteristics of observed double dominant frequency bands over increasing stress were compared. Furthermore, microscopic failure mechanism was revealed using the first motion polarity method.

2 Experimental Procedure and Data Processing

2.1 Sample Preparation

White marble samples were taken from Baoxing in southwestern China. Eight cylindrical samples, referred to as M1, M2, M3, M4, M5, M6, M11 and M12, were prepared with the required dimensions of $\Phi 50 \times H100$ mm. To eliminate the error of unknown large defects, a circumferential surface pre-crack with a width of 2 mm and a depth of 3 mm was made in the middle of each sample (Fig. 1b). These pre-cracks reduce the cross-sectional area of the samples in the middle and also result in a concentration of stress. This is equivalent to creating a known defect while causing no impact on the direct tension. Therefore, if there is neither an obvious defect nor any defect greater than the known defect, failure would occur easily along the cross section in uniaxial direct tensile tests.

2.2 Experimental Setup and Equipment

A rock mechanics test system (Model: MTS815 Flex Test GT) was employed for the direct tensile tests (Fig. 1b). A high-strength adhesive, JGN, was used to ensure a good connection between the caps and the samples. The capacity of the axial load transducer was 1000 kN. The axial displacement, as a control parameter, was measured with a linear variable differential transformer (LVDT), with a range of ± 2.5 mm. The loading rate was kept constant at 0.1 mm/min for testing Group 1, consisting of M1, M2 and M3, and at 0.05 mm/min for testing Group 2, consisting of M4, M5 and M6, and at 0.2 mm/min for testing Group 3, consisting of M11, M12.

A three-dimensional real-time monitoring system (Model: PCI-2), manufactured by American Physical Acoustic Corporation, was employed to automatically capture the AE waveforms. Eight micro30 sensors were installed symmetrically in the radial direction along the surface of the cylinder (Fig. 1b). The micro30 sensor has a good frequency response as well as good sensitivity to AE data, which facilitates the acquisition of waveform data, even in the presence of high background noise. The sampling frequency is 1 MHz, and the pre-amplification is 40 dB. Vaseline was used as a coupling agent for enhancing the connections between the sensors and the specimens.

2.3 Waveform Data Processing

AE waveforms were processed into a single data file (Fig. 1a) automatically by PCI-2; each data file recorded one fracture event by one AE waveform. Fast Fourier transformation (FFT) then was employed to analyze the available AE waveform data to obtain dominant frequency information conveniently and efficiently. With the help of a MATLAB programming process, all dominant frequencies were calculated through a batch process and exported to Excel (Fig. 1c) automatically. Corresponding loading times and stress states, as well as amplitudes, also were recorded in the Excel spreadsheet (Fig. 1c).

3 Experimental Results and Discussion

3.1 Fracture Surface Morphology

Following failure, the morphology of the fracture surface was investigated. Fracture surface initiation and propagation are dominated by the pre-crack until the onset of macroscopic failure, as shown in Fig. 2. This indicates that there is no error caused by any obvious defects under direct tensile tests among the six marble specimens, which is conducive to studying the characteristics of AE waveforms.

3.2 Frequency Characteristics

Figure 3 shows the dominant frequency distribution of AE waveforms corresponding to the normalized applied stress (σ/σ_t) throughout the whole process for the individual specimens of Group 1. The normalized loading stress is defined as the ratio of the applied stress (σ) to the peak stress (σ_t). Each mark in Fig. 3 indicates the dominant frequency of one AE waveform. Its density on the graph is directly associated with the AE activities that occurred on the fractured surface of the specimens during the loading process. For Group 1, the dominant frequency distribution reveals a similarity from the beginning to the final failure. Two dominant frequency bands are obvious (Fig. 3). The high dominant frequency band, referred to as the high band and marked by blue dots, is mostly distributed in a range between 200 and 268 kHz. The corresponding AE

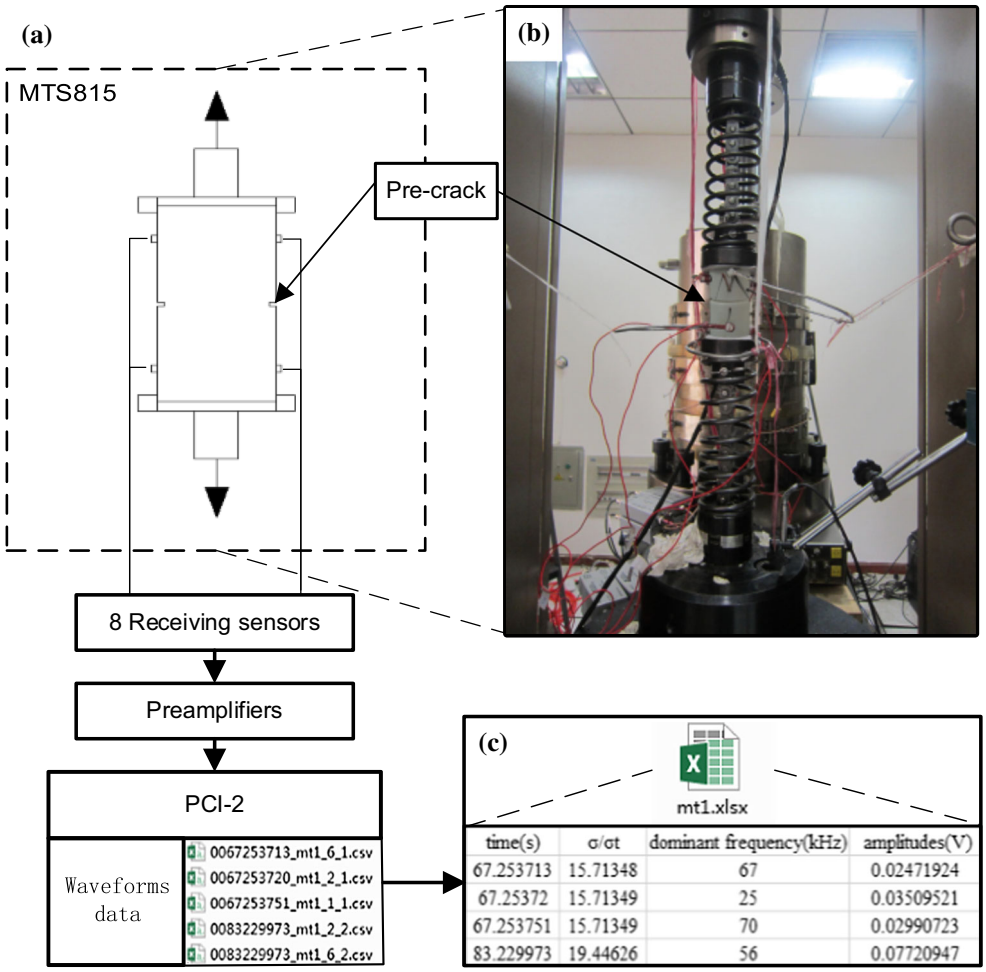

Fig. 1 **a** Schematic diagram of acquisition system and processing software; **b** loading system and specimens with array of sensors after test (*front view*); **c** AE signal waveforms processing results

waveforms are referred to as H-type waveforms. Similarly, the low dominant frequency band, referred to as the low band and marked by red dots, is between 14 and 86 kHz, and is related to L-type waveforms. Individual dominant frequencies beyond the two frequency bands are marked with black dots. Over 90% of the dominant frequencies are located in the two bands. Meanwhile, L-type waveforms are far more common than H-type ones, as shown in Table 1.

Further experiments have been undertaken to examine the effects at different loading rates. Figure 4 shows the dominant frequency distribution corresponding to the normalized applied stress (σ/σ_t) of Group 2 and Group 3. It clearly shows that the widths and ranges of the two dominant frequency bands are unacted at different loading rates during the transition from initiation of loading up to the application of ultimate stress. In addition, there is no obvious change in the number of AE waveforms. Similarly, dominant frequencies in the two bands account for over 90%, and L-type waveforms are still far more common than H-type ones, without a significant ratio change at different loading rates, as illustrated in Table 1.

Figure 5 shows the amplitude distributions of AE waveforms corresponding to the normalized applied stress (σ/σ_t) of the eight specimens. Red dots represent the AE waveforms with low band dominant frequencies; meanwhile, blue triangular symbols represent the AE waveforms with high band dominant frequencies. The amplitudes of AE waveforms in both the high- and low-frequency bands are observed to be small prior to the onset of peak stress. The AE waveform with the highest amplitude appears at the peak stress; meanwhile, many AE waveforms with high amplitudes are released. A remarkable feature is that all high-amplitude AE waveforms at the peak time are L-type waveforms, whereas all H-type waveforms represent small amplitudes over the entire loading process. The loading rate has no influence on the above feature.

Red and blue lines represent the cumulative increase of L-type and H-type waveforms, respectively, corresponding to the normalized applied stress (σ/σ_t), as shown in Fig. 6.

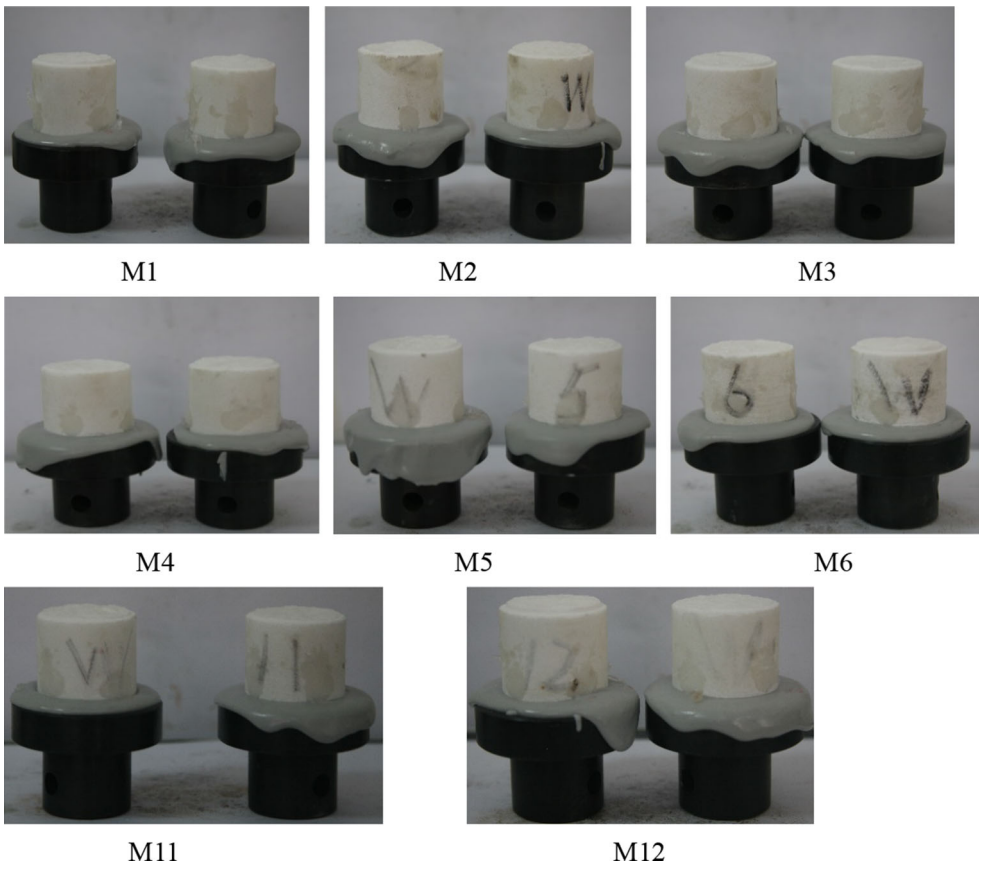

Fig. 2 Macroscopic failure morphology of white marble specimens

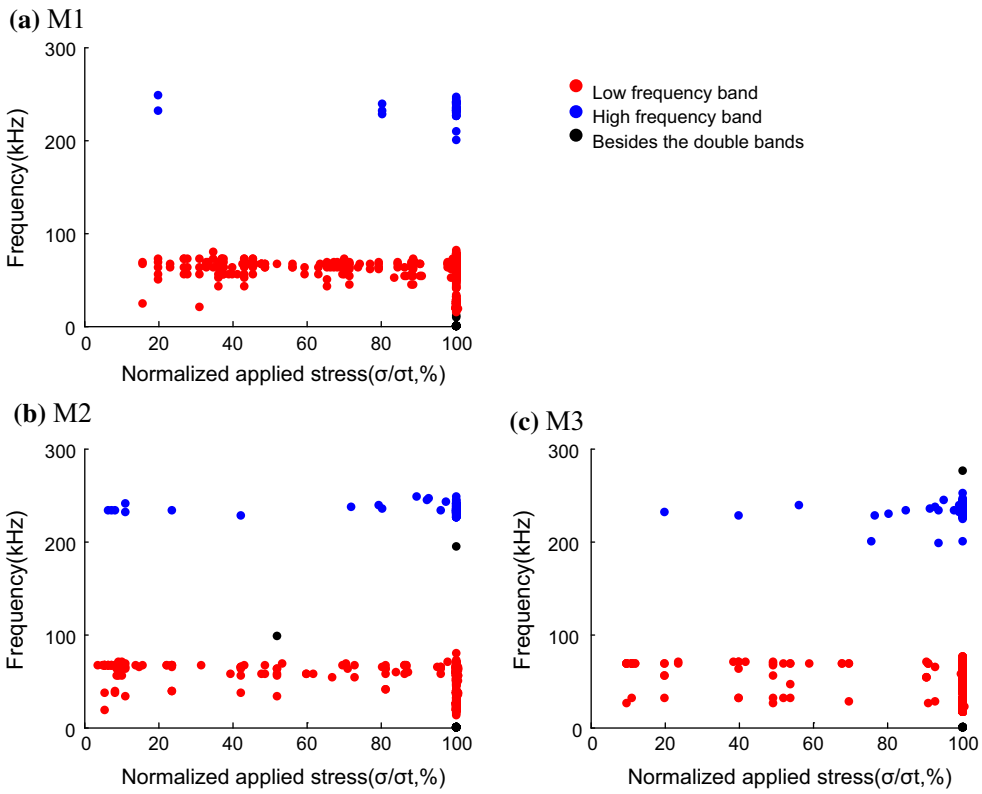

Fig. 3 Characteristic of dominant frequency versus the normalized loading stress for Group 1

Table 1 Principal properties of AE waveforms

Test type (loading rate)	Sample	σ_t (MPa)	N	R (%)	R_l (%)	R_h (%)
Group 1 (0.1 mm/min)	M1	3.28	650	95.69	88.62	7.07
	M2	3.43	824	96.48	85.56	10.92
	M3	3.7	798	99.88	85.44	14.44
Group 2 (0.05 mm/min)	M4	3.1	845	99.77	85.33	14.44
	M5	2.72	574	96.03	79.79	19.16
	M6	3.43	795	100	89.43	10.57
Group 3 (0.2 mm/min)	M11	3.27	768	94.66	86.07	8.59
	M12	3.36	845	95.03	78.46	16.57

σ_t stands for tensile strength, N the total number of AE signal waveforms, R the ratio of L-type waveforms and H-type ones to N, R_l the ratio of L-type waveform to N, R_h the ratio of H-type waveform to N

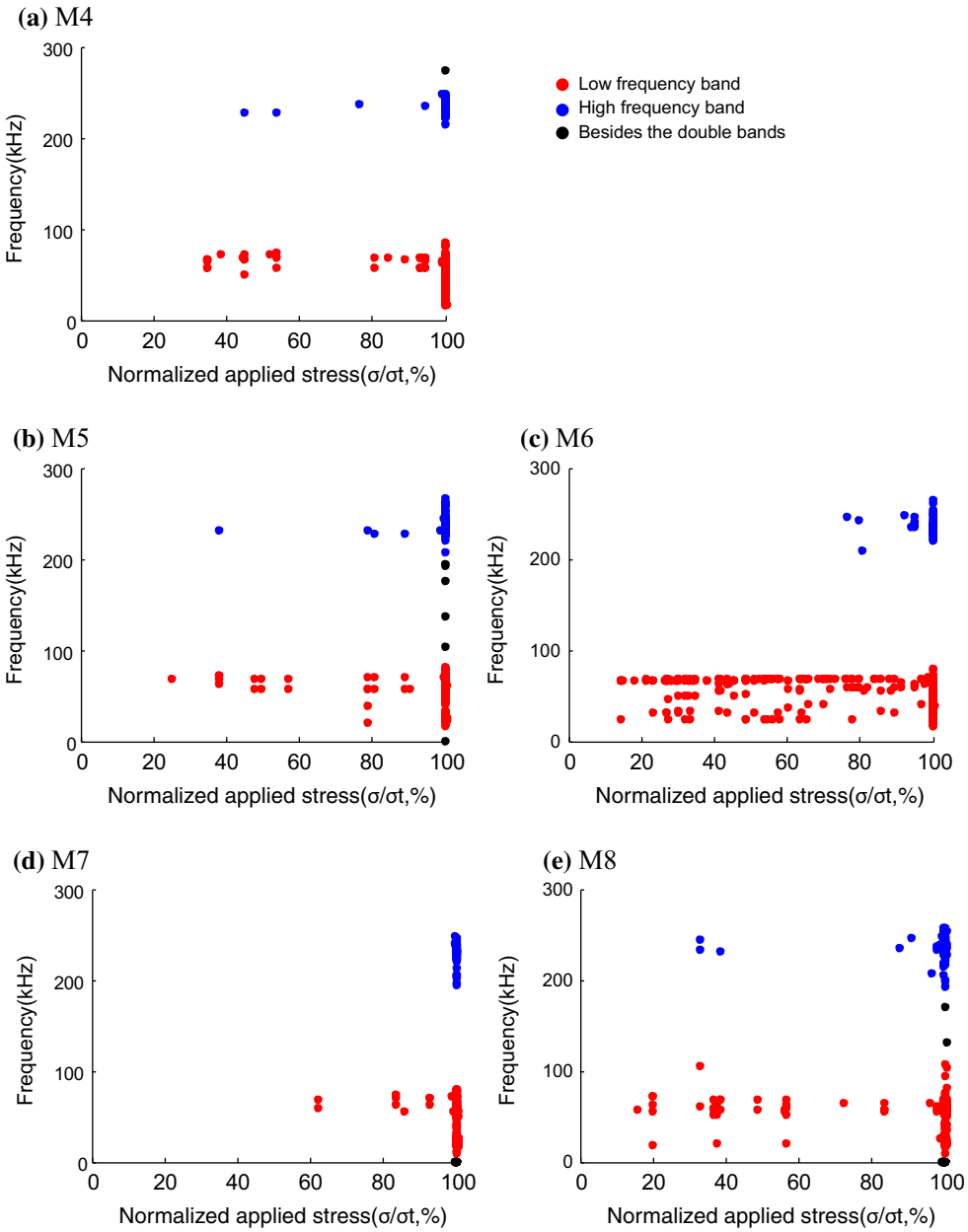

Fig. 4 Characteristics of dominant frequency versus normalized loading stress for Group 2

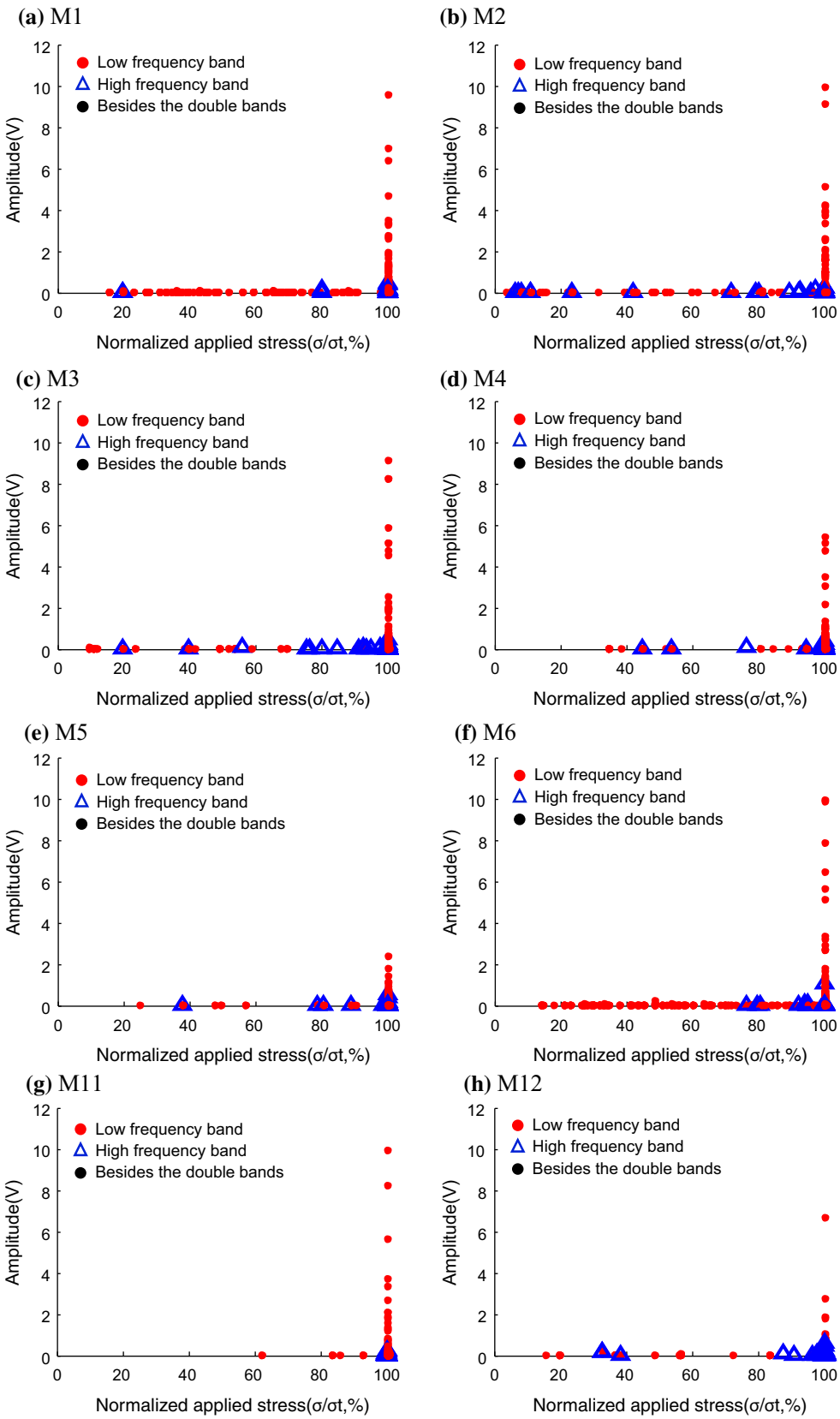

Fig. 5 Characteristics of amplitudes of signal waveforms versus normalized loading stress

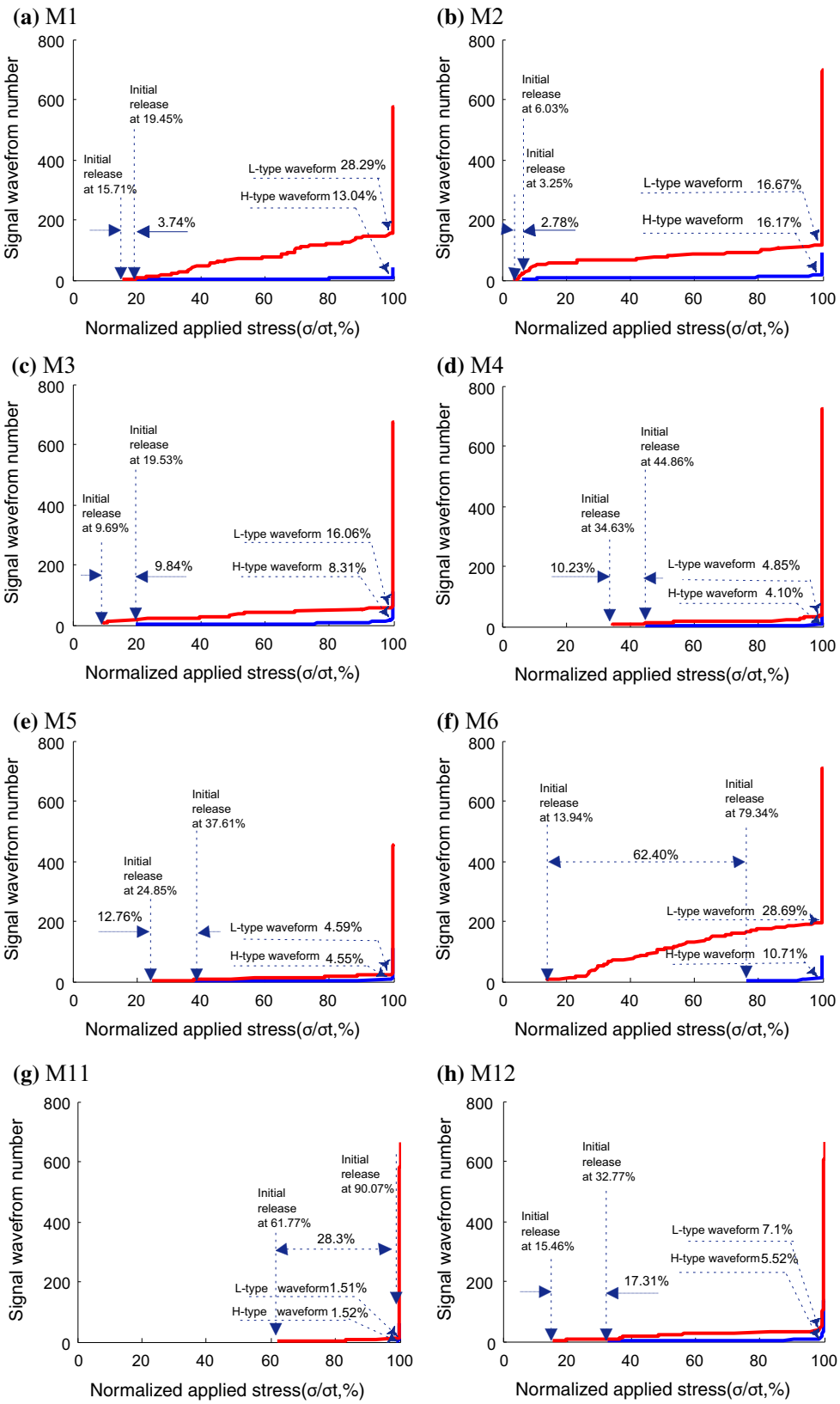

Fig. 6 Characteristic of cumulative increasing curve of H-type waveform and L-type waveform, respectively, corresponding to the normalized applied stress

A fascinating phenomenon is found where L-type waveforms are always detected prior to H-type ones in direct tensile tests. This phenomenon does not change with variations in the loading rate. However, the small change of loading rate does not reflect in the time intervals between the first releases of H- and L-type waveforms under static loadings. Moreover, when a higher proportion of L-type waveforms are released before reaching peak stress, they are accompanied by a higher proportion of released H-type waveforms, as shown in Fig. 6a–c, f. In contrast, when a lower proportion of L-type waveforms are released before reaching peak stress, they are accompanied by a lower proportion of released H-type waveforms, as shown in Fig. 6d–h. The figure shows that the generation of H-type and L-type waveforms follows and promotes each other during the entire loading process, even though H-type waveforms are relatively very rare.

3.3 AE Mechanism Analysis

AE source mechanisms were calculated by using the first motion polarity method (Zang et al. 1998). The polarity value of an event is calculated by:

$$\mathrm{Pol} = \frac{1}{K}\sum_{i=1}^{K} \mathrm{sign}(A_i), \tag{1}$$

where A is the first pulse amplitude and K is the number of channels used for hypocenter determination. It provides us with an estimate of the net polarity of the volume change at the location of the source. Classification is then carried out within three selected ranges, which are ascribed to the formation of different types of microscopic failure. AE is described as S-type events (shear) for a polarity between -0.25 and $+0.25$, T-type (tensile) for pol < -0.25, or C-type (collapse) for pol $> +0.25$. It has been used to evaluate the microscopic source mechanisms (Nasseri et al. 2006; Graham et al. 2010).

The more AE events there are, the more accurate mechanism analysis will become. Therefore, three samples, M2, M4, M12, were used to mechanism analysis. It is revealed that 63.16, 73.33, 65% of the total events were of tensile type, and 26.31, 20, 25% of the total events were of shear type for M2, M4, M12, respectively, as shown in Fig. 7. The failure mechanism of white marble is mainly tension failure under direct tensile tests, as well as less shear failure.

4 Discussion

H- and L-type waveforms accounted for over 95% of all AE waveforms observed and even 100% in one case. Furthermore, the amplitudes of AE waveforms for which the dominant frequency fell outside the two dominant

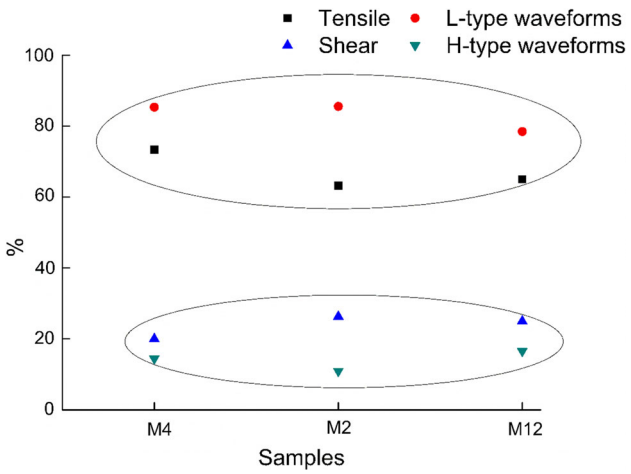

Fig. 7 Relationship between the ratio of dominant frequency characteristics and microscopic failure mechanisms

frequency bands are very small. Such AE waveforms appear neither frequently nor regularly, so in general they can be neglected during analysis. H- and L-type waveforms reinforce each other's generation and growth during the entire loading process. Therefore, the generation of H-type waveforms also provides an important AE signature corresponding to direct tensile fractures in marble, where H-type waveforms are relatively rare. Our results confirm that there is an obvious phenomenon of double dominant frequency bands for AE waveforms in marble exposed to direct tensile forces. L-type waveforms are always generated first and are far more abundant than H-type waveforms. This is another significant characteristic for white marble under direct tensile tests. The loading rate has no influence on the prominent feature described above under static load.

Frequency is uniquely determined by wave sources. Difference in frequency is a response to the difference in characteristics of wave source. Different microscopic fractures could be discriminated by different dominant frequency. AE source mechanism analysis reveals that the failure mechanism of white marble under direct tensile tests is mainly tension failure, as well as less shear failure. The ratio of L-type waveforms to total waveforms and the ratio of tensile type events to total events are compared, as well as the ratio of H-type waveforms to total waveforms and the ratio of shear type events to total events, as shown in Fig. 7. Therefore, the L-type waveforms should be produced due to tension failure, whereas the H-type waveforms should be caused by shear failure.

It can help understanding the characteristics of AE waveforms profoundly. Under tensile loading, microscopic tension failures are prone to occur at the preliminary stage of loading. It indicates that early detected L-type waveforms are related to tension failure. Few shear failures arise as a result of crack propagation under increased loadings

due to the complexity of rock microstructure. These shear failures are exhibited by H-type waveforms. Failures outbreak around reaching the peak stress and most of them are tension ones under direct tensile test since white marble is a typical brittle material. At this moment, it mainly reflects in L-type waveforms with large amplitudes.

Direct tensile loading is a relatively simple way to implement macroscopic loading. Therefore, the distribution of the dominant frequencies of white marble is worth examination under other loading condition as well. Furthermore, the relationship between the characteristics of AE waveforms and microscopic failure mechanism is worth to study further under other loading conditions. These two topics could lead to some interesting developments of future research.

5 Conclusions

Based on the results of direct tensile tests on white marble under different loading stresses, this paper has investigated the characteristics of the dominant frequencies of AE waveforms. Meanwhile, microscopic failure mechanism is briefly analyzed and discussed. The following conclusions can be drawn from the study.

1. Two dominant frequency bands of AE waveforms in white marble are revealed in the direct tensile tests. Their widths and ranges were unacted at different loading rates over the duration of the loading process. High and low dominant frequencies fall within the 200–268 and 14–86 kHz bands, respectively.
2. The AE waveforms associated with the low dominant frequency band make up the largest proportion of observed AE events, and they are always generated first under direct tensile conditions. Moreover, the highest amplitudes observed in the waveforms are always associated with low dominant frequencies.
3. The L-type waveforms are produced by tension failure, while the H-type waveforms are caused by shear failure.

Acknowledgements The authors are grateful for the financial support from the National Key Research and Development Plan (No. 2016YFC0600702), the National Program on Key Basic Research Project (Program 973, No. 2015CB057903), the National Natural Science Foundation of China (51509173).

References

Amann F, Button EA, Evans KF, Gischig VS, Blumel M (2011) Experimental study of the brittle behavior of clay shale in rapid unconfined compression. Rock Mech Rock Eng 44(4):415–430

Armstrong BH (1969) Acoustic emission prior to rockbursts and earthquakes. Bull Seismol Soc Am 59(3):1259–1279

Baddari K, Frolow AD, Tourtchine V, Rahmoune F (2011) An integrated study of the dynamics of electromagnetic and acoustic regimes during failure of complex macrosystems using rock blocks. Rock Mech Rock Engng 44(3):269–280

Behnia A, Chai HK, Shiotani T (2014) Advanced structural health monitoring of concrete structures with the aid of acoustic emission. Constr Build Mater 65(65):282–302

Butt SD (1999) Development of an apparatus to study the gas permeability and acoustic emission characteristics of an outburst-prone sandstone as a function of stress. Int J Rock Mech Min Sci 36:1079–1085

Chugh YP, Hardy RH Jr, Stefanko R (1968) Investigation of the frequency spectrum of microseismic activity in rock under tension. Basic Appl Rock Mech 4:73–113

Fleischmann P, Roudy D, Lakeestani F, Baboux JC (1975) A spectrum analysis of acoustic emission. Non-Destr Test 8(5):241–244

Graham CC, Stanchits S, Main IG, Dresen G (2010) Comparison of polarity and moment tensor inversion methods for source analysis of acoustic emission data. Int J Rock Mech Min Sci 47:161–169

Kranz RL (1979) Crack growth and development during creep of Barre granite. Int J Rock Meth Min Geomech Abstr 16:23–35

Lavrov A (2003) The Kaiser effect in rocks: principles and stress estimation techniques. Int J Rock Mech Min Sci 40:151–171

Liu JP, Li YH, Xu SD, Xu S, Jin CY, Liu ZS (2015) Moment tensor analysis of acoustic emission for cracking mechanisms in rock with a pre-cut circular hole under uniaxial compression. Eng Fract Mech 135:206–218

Lu CP, Dou LM, Zhang N, Xue JH, Wang XN (2013) Microseismic frequency-spectrum evolutionary rule of rockburst triggered by roof fall. Int J Rock Mech Min Sci 64(6):6–16

Moradian Z, Einstein HH, Ballivy G (2016) Detection of cracking levels in brittle rocks by parametric analysis of the acoustic emission signals. Rock Mech Rock Eng 49(3):1–16

Nasseri MHB, Mohanty B, Young RP (2006) Fracture toughness measurements and acoustic emission activity in brittle rocks. Pure Appl Geophys 163:917–945

Ohnaka M, Mogi K (1981) Frequency dependence of acoustic emission activity in rocks under incremental, uniaxial compression. Bull Earthq Res Inst 56:67–89

Ohnaka M, Mogi K (1982) Frequency characteristics of acoustic emission in rocks under uniaxial compression and its relation to the fracturing process to failure. J Geophys Res 87(B5):3873–3884

Prikry R, Lokajicek T, Li C, Rudajev V (2003) Acoustic emission characteristics and failure of uniaxially stressed granite rocks: the effect of rock fabric. Rock Mech Rock Eng 36(4):255–270

Read MD, Ayling MR, Meredith PG, Murrell SAF (1995) Micro cracking during triaxial deformation of porous rocks monitored by changes in rock physical properties, II. Pore volumometry and acoustic emission measurements on water-saturated rocks. Tectonophysics 245:223–235

Reiweger I, Mayer K, Steiner K, Dual J, Schweizer J (2015) Measuring and localizing acoustic emission events in snow prior to fracture. Cold Reg Sci Technol 110:160–169

Shukla R, Ranijith PG, Choi SK, Haque A, Yellishetty M, Hong L (2013) Mechanical behavior of reservoir rock under brine saturation. Rock Mech Rock Eng 46(1):83–93

Sondergeld CH, Getting IC, Spetzler HA, Sobolev G (1980) Observations of velocity changes during the deformation of pyrophyllite. Pure Appl Geophys 118:975–989

Stephens RW, Pollock AA (1971) Waveform and frequency spectra of acoustic emissions. J Acoust Soc Am 50:904–910

Tham LG, Liu L, Tang CA, Lee PKK, Tsui Y (2005) On tension failure of 2-D rock samples and associated acoustic emission. Rock Mech Rock Eng 38(1):1–19

Woodward B (1976) Identification of acoustic emission source mechanisms by energy spectrum analysis. Ultrasonics 14(6):249–255

Xie HP, Liu JF, Ju Y, Li J, Xie LZ (2011) Fractal property of spatial distribution of acoustic emissions during the failure process of bedded rock salt. Int J Rock Mech Min Sci 48:1344–1351

Xu XF, Dou LM, Lu CP, Zhang YL (2010) Frequency spectrum analysis on micro-seismic signal of rock bursts induced by dynamic disturbance. Min Sic Technol 20:0682–0685

Zang A, Wagner C, Stanchits S, Dresen G, Andresen R, Haidekker MA (1998) Source analysis of acoustic emissions in Aue granite cores under symmetric and asymmetric compressive loads. Geophys J Int 135:1113–1130

Zhang R, Dai F, Gao MZ, Xu LW, Zhang CP (2015) Fractal analysis of acoustic emission during uniaxial and triaxial loading of rock. Int J Rock Mech Min Sci 79:241–249

Zhang J, Peng W, Liu F, Zhang H, Li Z (2016) Monitoring rock failure processes using the Hilbert–Huang transform of acoustic emission signals. Rock Mech Rock Eng 49(2):427–442

Zhao XG, Cai M, Wang J, Ma LK (2013) Damage stress and acoustic emission characteristics of the Beishan granite. Int J Rock Mech Min Sci 64:258–269